FULL PAPER

Ultrafast Self-Assembly of Graphene Oxide-Induced Monolithic NiCo–Carbonate Hydroxide Nanowire Architectures with a Superior Volumetric Capacitance for Supercapacitors

Juan Yang, Chang Yu,* Xiaoming Fan, Changtai Zhao, and Jieshan Qiu*

The monolithic electrodes with high volumetric capacitance demonstrate a great potential in practical industrial applications for supercapacitors. Herein, a novel strategy for ultrafast self-assembly of graphene oxides (GO)-induced monolithic NiCo–carbonate hydroxide (NiCo–CH) nanowire composite films (G–CH) is reported. The oxygen-containing functional groups on the GO surface help effectively to induce formation of the monodisperse NiCo–CH nanowires. Such a nanowire-shaped structure further functions as a scaffold and/or support, leading to 25 s of ultrafast self-assembly for G–CH composite films and a relatively loose and open channel that contributes to fast electrolyte transport. The as-obtained monolithic G–CH architectures show an excellent supercapacitor performance as binder- and conductive agent-free electrode, evidenced by a superior volumetric capacitance of 2936 F cm^{-3} and good electrochemical stability. Combining highly conductive carbon nanotubes (CNTs) into the monolithic composite films can further create well-interconnected conductive networks within the electrode matrix, thus to improve the reaction kinetics and rate capability. The present strategy that can modulate the growth of the high-electroactive pseudocapacitive hydroxides and achieve an ultrafast self-assembly of monolithic composites may pave a promising new way for development of high-performance supercapacitors and shed a new light on the configuration of carbon-based electrode materials in energy storage and conversion devices.

1. Introduction

The rapid development of electronic devices and hybrid electric vehicles has stimulated the increasing demand for high energy storage systems.[1–5] In particular, supercapacitors with both high power density and long cycle life hold a great promise in the future electrical energy storage fields.[6,7] The

high performance of the supercapacitors strongly relies on the rational design of novel monolithic electrode materials, which is easy to fabricate and simple to operate, with an aim of effectively reducing the "dead surface" in traditional slurry-derived electrodes, and this will help to facilitate more efficient charge and mass transportations.[2,8,9] Recent advances in monolithic and even flexible electrodes have been demonstrated and fast driven by highly conductive graphene self-assembled 2D films and 3D aerogel.[10–15] However, the agglomeration/restacking of graphene sheets and intrinsic limitation of the electrostatic surface charging mechanism involved in the process reported so far tend to result in a severely decreased specific surface area and unsatisfactory capacitive performance that is below the requirement from the practical applications. In particular, the graphene-based monolithic electrode materials available now have a relatively low volumetric capacitance, and this is an obvious drawback and a remaining challenge to be tackled from a view point of both theoretical study and practical applications of supercapacitors.

Pseudocapacitor-type electrode materials involving multiple oxidation states for the fast reversible Faradaic reactions can deliver very high specific capacitance, as evidenced by the transition metal oxides/hydroxides, and conducting polymers.[16–20] It has been found that the electrochemical performance of these materials can be further improved by coupling carbon species within the electrode matrix.[21–24] A novel monolithic composite with alternate connections of pseudocapacitive species and graphene nanosheets, has been envisioned as a new protocol, and has triggered an avalanche attention due to the extraordinary storage, transport, and mechanical performance.[25–28] Up to now, a number of strategies have been developed to assemble or anchor active pseudocapacitive species onto the graphene materials to fabricate the monolithic composite electrodes such as directly mixing with the graphene oxides (GO), and the in situ nucleation and growth on the graphene monoliths.[26,29–31]

J. Yang, Dr. C. Yu, Dr. X. Fan, C. Zhao, Prof. J. Qiu
Carbon Research Laboratory
Liaoning Key Lab for Energy Materials
and Chemical Engineering
State Key Lab of Fine Chemicals
Dalian University of Technology
Dalian 116023, China
E-mail: chang.yu@dlut.edu.cn; jqiu@dlut.edu.cn

Thereinto, pseudocapacitive species function as a "spacer" that has dual roles: to effectively mitigate the self-aggregation and restacking of graphene and to boost the volumetric density of electrodes and deliver the high electrochemical performance. Nevertheless, unique function and role of GO, especially oxygen-containing functional groups on GO surface for growth of pseudocapacitive species was commonly ignored and never unveiled in detail, moreover, time-consuming assembly process limits the practical application of monolithic composites. Therefore, a simple yet effective strategy that can modulate the growth of the pseudocapacitive species and the in situ ultrafast self-assembly of graphene for monolithic electrodes with tuned structure and properties is still highly demanded.

The bimetallic NiCo–carbonate hydroxides (NiCo–CH), possessing rich redox reaction sites, have been widely used as a precursor to synthesize mixed transition metal oxides with pseudocapacitive behaviors, such as spinel-type $NiCo_2O_4$ or NaCl-type $Ni_xCo_{1-x}O$ ($0 < x < 1$), but their own pseudocapacitive behaviors are not widely concerned.[32,33] It is also found that such NiCo–CH species can be readily shaped into multiform morphologies, such as nanowires, nanosheets, and other oriented nanostructures in comparison to other NiCo-based hydroxides.[32,34] The tailored characteristics will be favorable for revealing the corresponding relation between electrode structure and electrochemical performance. Herein, we report a strategy for ultrafast self-assembly of the monolithic composite films (G–CH) with alternate connections of the monodisperse bimetallic NiCo–CH nanowires and graphene nanosheets by a facile hydrothermal technique followed by vacuum filtration. The GO is responsible for the formation of monodisperse NiCo–CH nanowires, with the oxygen-containing functional groups on the surface functioning as anchoring sites for inducing crystal seed nucleation and growth. The NiCo–CH nanowires function as a scaffold and/or support, being responsible for 25 s fast self-assemble, thus leading to relatively loose and open channels. These two simultaneous interactions combine together to result in the ultrafast self-assembly of the film-like G–CH composites. The as-obtained G–CH composite films are evaluated as binder- and conductive agent-free electrodes in supercapacitors, exhibiting a superior volumetric density, a high specific capacitance, and a good electrochemical stability. The incorporated carbon nanotubes (CNTs) help to further improve the electrical conductivity of the composite films, facilitate the charge transfer, and enhance the reaction kinetics, thus delivering an enhanced rate performance of the G–CH composite films.

2. Results and Discussion

2.1. Fabrication of the GO-Induced Monolithic NiCo–CH Composite Films

The fabrication process of GO-induced monolithic NiCo–CH architectures is illustrated in **Figure 1**. The free nucleation and
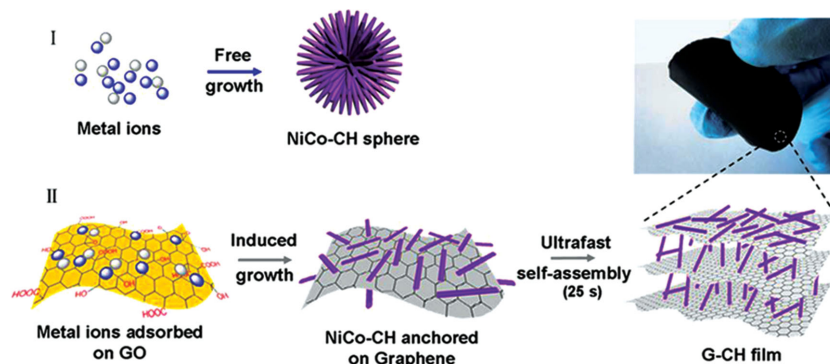

Figure 1. Schematic of the fabrication process for GO-induced monolithic NiCo–CH composite films: I) Free nucleation and growth process, leading to spheres made of microsized NiCo–CH nanowires, and none monolithic materials; II) GO-induced nucleation and growth of NiCo–CH nanowires anchored on graphene and ultrafast self-assembly to monolithic G–CH architectures (in about 25 s), exhibiting an excellent flexibility.

growth of NiCo–CH seeds in the absence of GO would result in sphere-like aggregation structures made of microsized NiCo–CH nanowires, which is difficult to control to obtain monolithic materials (process I). Nevertheless, it is interesting to note that monodisperse NiCo–CH nanowire structures are formed in the GO colloidal solution, highlighting the unique function of the GO. It is believed that the GO with abundant oxygen-containing functional groups function effectively to induce the nucleation and growth of NiCo–CH crystal seeds on the GO surface. The NiCo–CH nanowires anchored on graphene sheets further function as a scaffold and/or support, resulting in self-assembled monolithic G–CH composite films with relatively loose and open channels. The self-assembly step can be finished quickly in 25 s, of which the detailed information for process II can be found in Figure 1 and Movie S1, Supporting Information. Such a unique and effective process is rarely achieved in NiCo-compounds/graphene composites reported previously.[28,35] The G–CH composite films can also further be modulated to make G–CH–CNT composite films by incorporating conductive CNTs into the G–CH dispersion solution, in which the incorporated CNTs function as a conducting framework to further improve the electrical conductivity of the concerned composite films.

The typical field-emission scanning electron microscopy (FE–SEM) images of the sphere-like NiCo–CH species from the free nucleation and growth of seeds in the absence of GO are shown in **Figure 2**a and Figure S1, Supporting Information. The sphere-shaped NiCo–CH species have a diameter of ≈7 μm and are composed of numerous small nanowires radially grown from the center. Surprisingly, in sharp contrast with the microsized NiCo–CH sphere, the uniform and monodisperse NiCo–CH nanowires can be clearly observed when the GO is present (Figure 2b,c, the top-view FE–SEM images of monolithic G–CH films). This kind of monolithic G–CH architectures (inset, Figure 2b) made of NiCo–CH nanowires and graphene nanosheets have a high volume density of ≈2.1 g cm^{-3} (Figure S2, Supporting Information). It is believed that the oxygen-containing functional groups on the GO surface, such as hydroxyl and carbonyl groups, would act as anchoring sites for inducing nucleation and growth of the NiCo–CH seeds, leading
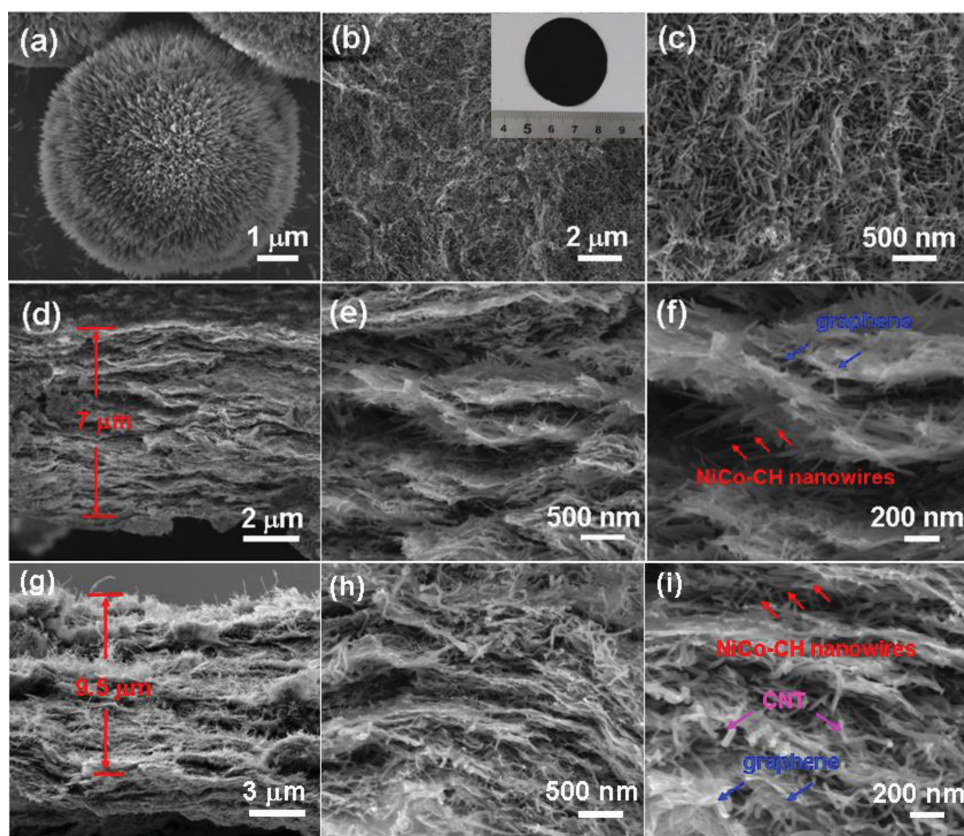
www.MaterialsViews.com

ADVANCED
FUNCTIONAL
MATERIALS
www.afm-journal.de

FULL PAPER

Figure 2. Morphologies of the samples: a) FE–SEM image of the microsized NiCo–CH spheres in the absence of GO; b,c) top-view FE–SEM images of the self-supporting G–CH films; d–f) cross-section FE–SEM images of monolithic G–CH composite films; g–i) cross-section FE–SEM images of monolithic G–CH–CNT composite films.

to different structures between the NiCo–CH and G–CH products. The Figure 2d shows a FE–SEM image of the cross-section of the monolithic G–CH composite films, showing clearly that a layered structure of the G–CH composite films with an average thickness of ≈7 μm. Further high-resolution FE–SEM images reveal an alternate connected structure made of NiCo–CH species and the graphene nanosheets, in which NiCo–CH nanowires (red arrows) with a diameter of 10–15 nm are uniformly deposited on both sides of graphene sheets, and act as scaffolds and/or support (Figure 2e,f). These components combine together, and result in the composite films with a relatively loose and open channel, in which the layer distance of graphene sheets is extended to some degree (Figure 2d,e). The graphene sheets with high surface area exposed make it possible for high loading of NiCo–CH nanowires (≈93.7%, based on thermogravimetric analysis (TGA), Figure S3, Supporting Information) in the composite films. It should be also noted that in the presence of conducting CNTs with a mass ratio of ≈20% in the composite film (Figure S3, Supporting Information), the thickness of the concerned film increases from 7 μm for G–CH films to ≈9.5 μm for G–CH–CNT films (Figure 2g). The high-resolution FE–SEM images reveal that the CNTs are distributed uniformly within the matrix of the G–CH architectures (Figure 2h,i), which is also confirmed by FE–SEM images of the top-view of the monolithic G–CH–CNT films (Figure S4, Supporting Information).

The typical X-ray diffraction (XRD) patterns of the monolithic G–CH composite films and NiCo–CH spheres are shown in **Figure 3**a, in which the diffraction peaks at 2θ of 9.6°, 17.1°, 26.2°, and 39.3° corresponding to (110), (020), (220), and (231) plane reflections of Co–CH standard pattern, e.g., $Co(CO_3^{2-})_{0.5}OH \cdot 11H_2O$ (JCPDS Card no. 48-0083), can be clearly seen.[34,36] It is also noted that all the diffraction peaks slightly shift to the low diffraction direction, which is attributed to the partial substitution of Co ions by Ni ions in the Co–CH.[37] And it is also found that the crystal structure of the NiCo–CH species in the G–CH composite films keeps unchanged in the presence of GO. The diffraction peak at ≈10.0° corresponding to GO in the G–CH composite films disappears completely after the hydrothermal reaction, which is due to the GO reduction in the presence of urea.[38] The Raman spectra of pristine graphene sheets and the G–CH composite films are shown in Figure 3b. Compared with the pristine graphene sheets, the I_D/I_G ratio of the G–CH composite films increases slightly from 1.05 to 1.11, indicative of more structural defects on the graphene sheets, which obviously is related to the anchoring of NiCo–CH nanowires on the graphene surface.[39,40] Figure 3c is the Fourier transform IR (FT-IR) spectra of the as-prepared samples, in which the broad peaks centering at 3500 and 1630 cm^{-1} corresponding to the O–H stretching vibration of water molecules and the hydrogen bonding among the hydroxyl groups can be clearly seen for all the samples. The peaks at 1500
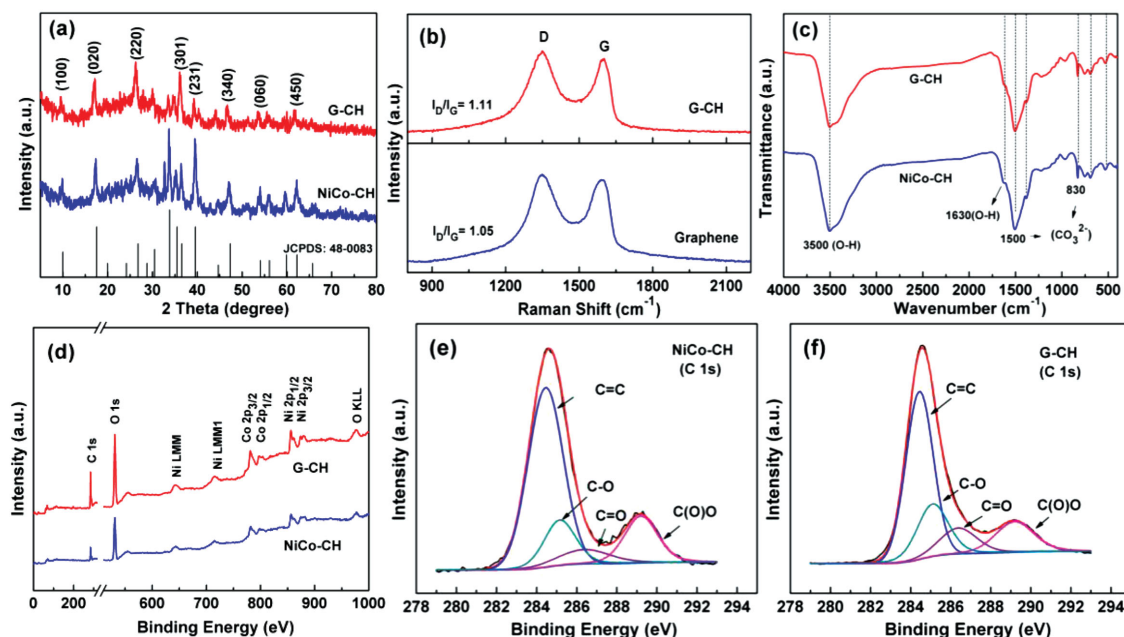
FULL PAPER

ADVANCED
FUNCTIONAL
MATERIALS
www.afm-journal.de

Materials Views
www.MaterialsViews.com

Figure 3. Structure characterization of the samples: a) typical XRD patterns of NiCo–CH spheres and the G–CH composite films; b) Raman spectra of graphene and G–CH composite films; c) FT-IR spectra of NiCo–CH spheres and G–CH composite films; d) XPS survey spectra; and e,f) high-resolution XPS spectra Ni 2p, Co 2p of NiCo–CH spheres and G–CH composite films.

and 830 cm^{-1} are attributed to the CO$_3^{2-}$ anions. The peak at 1617 cm^{-1} related to the nanostructured carbon in the G–CH sample was not found, which may be overlapped by the broad peak at 1630 cm^{-1} originated from the vibration of the adsorbed water molecules. Other peaks below 800 cm^{-1} are assigned to metal-oxygen (M–O–H) stretching and bending modes.[21,23,41] These results further confirm the formation of NiCo–carbonate hydroxides species in the G–CH composite films.

In order to obtain more information about the components and the surface electronic states of monolithic G–CH composite films, the composites were further examined by X-ray photoelectron spectroscopy (XPS) spectroscopy, of which the results are shown in Figure 3d. It can be clearly seen that the Ni, Co, C, and O elements are the main components of the NiCo–CH and G–CH composite films. The molar ratio of Ni to Co in the NiCo–CH and G–CH composites is calculated to be 1:1, close to that in the reactant mixture (Table S1, Supporting Information), further confirming that the components of NiCo–CH species in G–CH composites remain unchanged even in the presence of GO. For the C1s XPS spectra of NiCo–CH and G–CH composites, the spectra can be fitted and divided into four peaks: the aromatic linked carbon (C=C, 284.6 eV); the C in oxygen single-bonded carbon bonds (C–O, 285.1 eV); the carbonyl carbon (C=O, 286.3 eV), and the carboxylate carbon (O–C=O, 288.1 eV) (Figure 3e,f).[40,42] The percentage of those functional groups on the G–CH composite surface is slightly higher than that of the NiCo–CH (Table S2, Supporting Information), implying that some oxygen-containing functional groups are still present on the graphene surface under the hydrothermal conditions, which is beneficial to anchoring NiCo–CH nanowires on graphene. The high-resolution XPS spectra of Ni 2p (Figure S5a, Supporting Information) shows the two major peaks around 873.5 and 855.9 eV with a spin-energy separation of 17.6 eV due

to the presence of Ni^{2+}.[21,39] This is also the case for Co 2p XPS spectra, with the only difference in the binding energy of major peaks and the spin-energy separation, which is attributed to the presence of Co^{2+} (Figure S5b, Supporting Information).[18,34] These species will play a role for the high electrochemical performance of electrode materials.

To have an insight into the morphology and structure of the as-made G–CH composites, the composite films were further examined by transmission electron microcopy (TEM) and high-resolution TEM (HR–TEM), of which the typical images are shown in **Figure 4**. The low-magnification image shows the uniform distribution of NiCo–CH nanowires on the graphene surface, which is due to the GO-induced nucleation and growth of NiCo–CH crystal seeds (Figure 4a). The length of the nanowires is ≈200 nm, with a diameter of 10–15 nm (Figure 4b). A typical nanowire with visible lattice fringes can be distinctly observed in a HR–TEM image (Figure 4c), with a lattice spacing of ≈0.23 nm that can be indexed to the (231) plane of the NiCo–CH phase. In the case of the G–CH–CNT composites, a homogeneous nanostructure can be obtained due to the π–π interaction between CNTs and graphene sheets (Figure 4d). An enlarged view (Figure 4e,f) further reveals that the CNTs as conductive species in the network are distributed uniformly within the matrix of the G–CH composites, which is in agreement with the SEM results as discussed above. Scanning TEM (STEM) image and corresponding elemental mapping from the square region marked in Figure 4g further reveal a uniform distribution of NiCo–CH nanowires on the graphene sheets. All of the information available now has confirmed that the NiCo–CH nanowires are intimately anchored to the graphene sheets with a uniform distribution via a strong coupling interaction between the NiCo–CH nanowire and the graphene sheets.
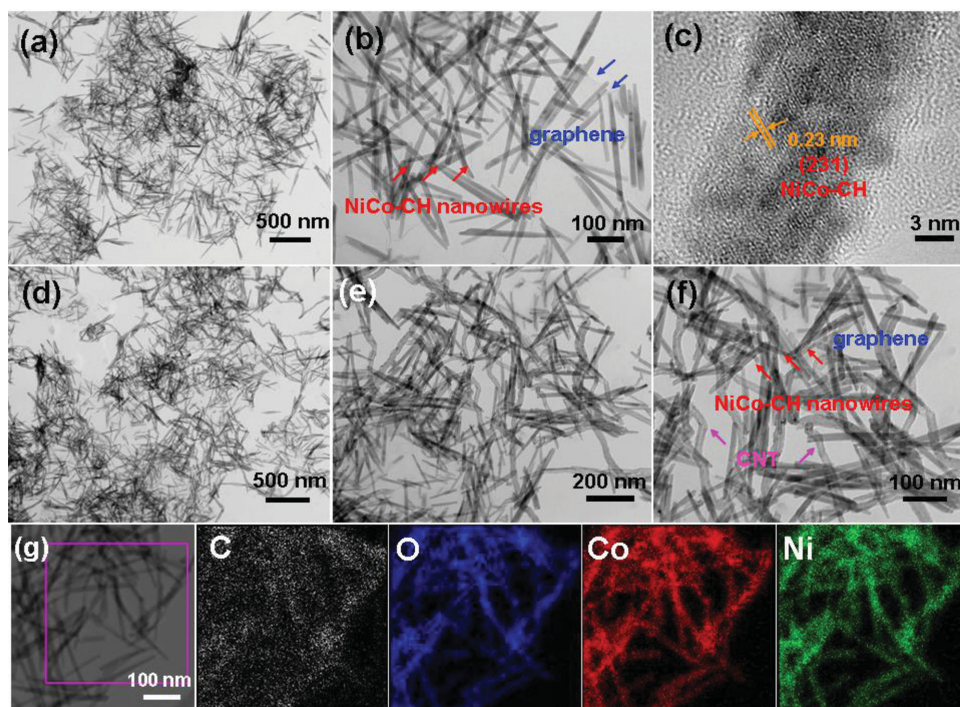
Figure 4. Morphology and structure characterization of samples: a,b) TEM and c) HR–TEM images of the G–CH composites; d–f) TEM images of the G–CH–CNT composites; and g) STEM image and corresponding elemental mapping of C, O, Co, and Ni from the square region marked in g), revealing the uniform distribution of NiCo–CH nanowires on the graphene sheets.

2.2. Electrochemical Performance of the GO-Induced Monolithic NiCo–CH Composite Films

The electrochemical performance of the monolithic G–CH composite films as binder-free and conductive-agent-free electrodes was evaluated in a three-electrode cell in 6 M KOH aqueous electrolyte. The cyclic voltammetry (CV) curves of the G–CH composite films at scan rates ranging from 5 to 50 mV s^{-1} are shown in **Figure 5**a. It can be seen that all of the CV curves have similar shapes and exhibit a set of intense redox peaks, indicating that the specific capacitance is primarily attributed to the fast and reversible electrochemical redox reactions.[18,23,43] In order to improve the rate capability of the composite film electrodes, the conductive CNTs were incorporated into the monolith to make G–CH–CNT composite films that show an increased CV curve area compared to that of G–CH electrode without CNTs at high scan rates (Figure 5b), implying a significantly improved rate capability for the G–CH–CNT films. This can be attributed to enhanced electrical conductivities (16.8 S m^{-1} for G–CH–CNT vs 4.2 S m^{-1} for G–CH film, Figure S6, Supporting Information) and charge transfer rate, which is confirmed by the kinetic process of the two electrodes as shown in Figure 5c. One can see clearly that the slope of the linear plot (the log peak current density vs the log scan rate) of G–CH–CNT is higher than that of the G–CH composite film, indicative of a fast charge and ion transport rate. It is noteworthy that both slopes of the G–CH and G–CH–CNT composites are smaller than 1, which is mainly attributed to the ohmic contributions.[7,44]

The specific capacitance of the G–CH composite films based on the charge-discharge curves (Figure S6a,b, Supporting Information) is shown in Figure 5d, showing clearly that the G–CH composite electrode yields both a high specific capacitance of 1398 F g^{-1} and a high volumetric capacitance of 2936 F cm^{-3} (based on the electrode volume density of ≈2.1 g cm^{-3}) at a current density of 1 A g^{-1}. These results are comparable to the data reported in literatures.[26,29,45,46] The possible reason behind this is that a relatively loose and open channel within the electrode matrix provides efficient and fast transport pathways for the electrolyte ions to the active material surface. It can maintain 588 F g^{-1} at 30 A g^{-1} with a capacitive retention rate of 42%, and the specific capacitance of G–CH can reach to 206 F g^{-1} at a current density as high as 100 A g^{-1}. The monolithic G–CH–CNT composite films also exhibit a specific capacitance of 1146 F g^{-1} at a current density of 1 A g^{-1}, and 462 F g^{-1} even at 100 A g^{-1} with an excellent capacitance retention rate of 40% (based on the charge-discharge curves in Figure S6c,d, Supporting Information), indicative of an enhanced rate capability compared to the G–CH composite films. This is also in good agreement with the CV results. To our best knowledge, such a superior electrochemical performance has been rarely before observed for monolithic composite materials.[45,47,48] For comparison, a slurry-derived powder electrode (G–CH–P) was made by pressing a mixture of the G–CH composite powder, carbon black and binder with a mass ratio in the electrode of ≈80:15:5 on a piece of nickel foam and evaluated under similar conditions. The G–CH–P electrode shows a specific capacitance of 984 F g^{-1} (based on the total electrode mass) at 1 A g^{-1}, which

**ADVANCED
FUNCTIONAL
MATERIALS**

www.afm-journal.de
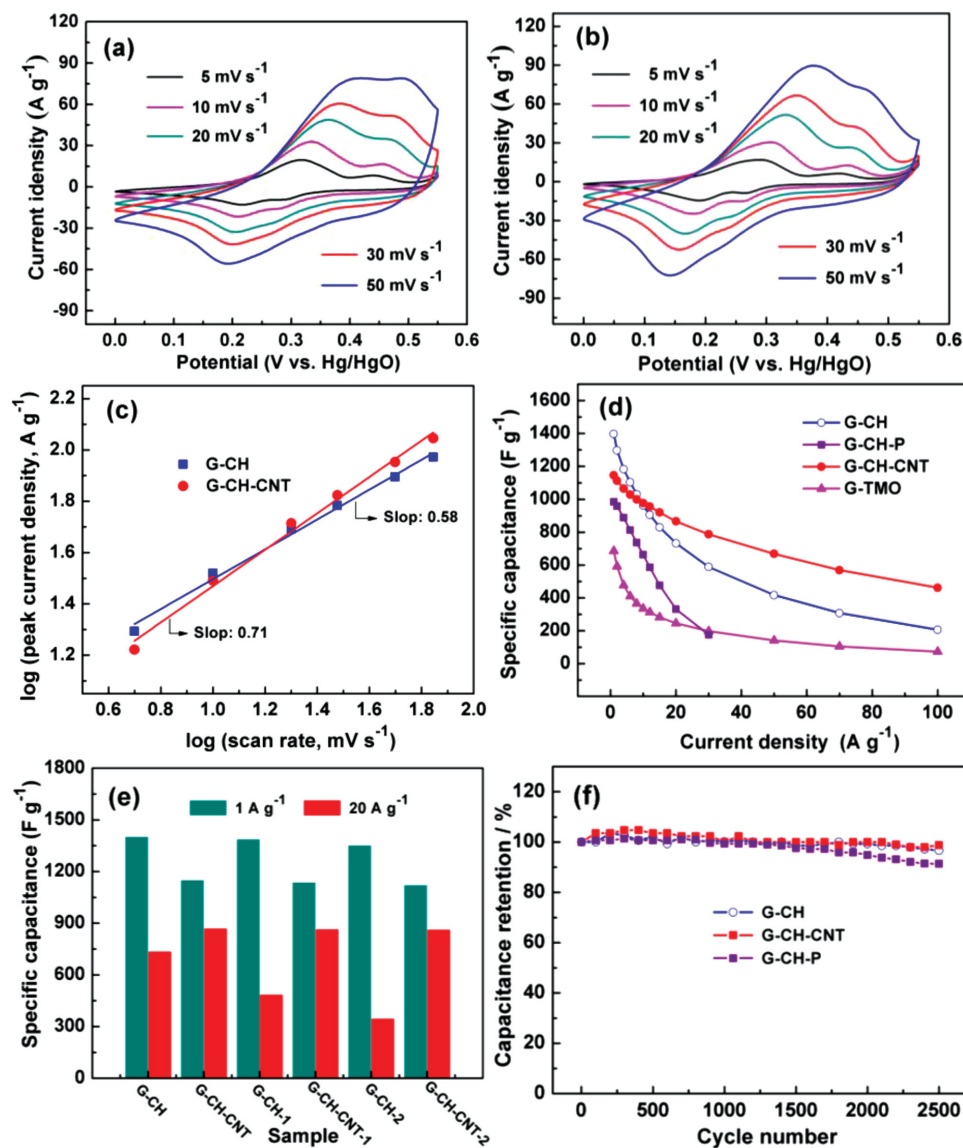
*Materials
Views*

www.MaterialsViews.com

Figure 5. Electrochemical performance of the samples for supercapacitors: a,b) CV curves of the monolithic G–CH and G–CH–CNT composite film at different scan rates ranging from 5 to 50 mV s^{-1}; c) relationship between anodic peak current and scan rates for the monolithic G–CH and G–CH–CNT composite film ($R^2 = 0.99$); d) the specific capacitance of the G–CH, G–CH–CNT, corresponding G–TMO composite films and slurry-derived electrode (G–CH–P) in the presence of conductive agents and binders at different current densities; e) relationship between specific capacitance and current density for different samples; and f) cycling performance of different samples at a current density of 6 A g^{-1}.

maintains only at 175 F g^{-1} at 30 A g^{-1} with a low capacitive retention rate of 18%, which is far lower than that of the G–CH (≈42%) and G–CH–CNT (≈69%) monolithic electrode (Figure 5d). This is due to the poor electrical conductivity of the slurry-derived electrode because the added conductive-agent and binder tend to result in low specific capacitance and slow transportation of charge and ions. For comparison, the G–CH composite film was further heated at high temperatures (350 °C), yielding transition metal oxide composite films (graphene-transition metal oxide, G–TMO). It has been found that in comparison with the G–TMO, both the G–CH and G–CH–CNT composite films show a notable enhancement in the specific capacitance (Figure 5d), which may be attributed to the

low crystallinity and better wettability of NiCo–CH species in electrolyte than the transition metal oxides.[49]

To further evaluate the electrochemical performance of the composite films, the specific capacitance of the G–CH films with different areal densities was investigated. The starting thickness of the G–CH composite film was fixed at an areal density of 1.5 mg cm^{-2}. The areal density can be turned from 2.2 to 3.0 mg cm^{-2} by changing the volume of G–CH composite solution in the vacuum filtration step, yielding two samples labeled as G–CH-1 and G–CH-2. The samples made in the presence of CNT were labeled as G–CH–CNT, G–CH–CNT-1, and G–CH–CNT-2. As shown in Figure 5e, the specific capacitance of the G–CH composite films at a low current density of

www.MaterialsViews.com

ADVANCED
FUNCTIONAL
MATERIALS
www.afm-journal.de

FULL PAPER

1 A g^{-1} varies slightly as the areal density increases. Nevertheless, as the areal density increases, the corresponding specific capacitance drops from 732 F g^{-1} at 1.5 mg cm^{-2} to 342 F g^{-1} at 3.0 mg cm^{-2} at a high current density of 20 A g^{-1}, indicative of thickness-dependent performance. This may be because that a high areal density hinders the transportation of the charge carriers to the active material surface to an extent, confirmed by the electrochemical impedance spectroscopy (Figure S6e, Supporting Information). It is interesting to note that in the case of G–CH–CNT composite film, the thickness-dependent behavior is not observed. The possible reason for this is that the CNTs within the composite matrix function as the conducting agent for the fast charge transfer, which helps to further enhance rate capability of G–CH composite films (Figure S6e,f, Supporting Information). The excellent electrochemical stability of the samples is further evidenced by the capacitance retention at 6 A g^{-1} for 2500 cycles (Figure 5f). For the G–CH and G–CH–CNT composite films, the specific capacitance can retain ≈95% of the highest value after 2500 cycles, which is better than the slurry-derived electrode G–CH–P (90%), demonstrating the excellent long term electrochemical stability that is highly demanded in practical applications.

3. Conclusions

We have reported a novel strategy for ultrafast self-assembly of monolithic G–CH architectures with alternate connections of the monodisperse NiCo–CH nanowires and graphene nanosheets by a facile hydrothermal step and a vacuum filtration step. The GO functions to induce the seed nucleation, formation and growth of the monodisperse NiCo–CH nanowires. The as-formed monodisperse NiCo–CH nanowires within graphene nanosheets matrix act as a scaffold and/or support to protect from aggregation or restacking of graphene, leading to relatively loose and open channels, thus an ultrafast self-assembly of the G–CH composites can be high efficiently achieved. Benefiting from the unique structure, the G–CH composite films show a highly volumetric density, a superior volume specific capacitance, and an excellent cycle abilities. An improved rate performance can be further achieved by incorporating conductive CNTs within the G–CH composite films. The present work provides a simple yet efficient way for configuring the monolithic electrode materials with a loose and open channel for energy storage devices.

4. Experimental Section

Fabrication of the Monolithic G–CH Composite Films: GO were synthesized by the modified Hummers method as described in the literature.[50] NiCl$_2$·6H$_2$O (180 mg), CoCl$_2$·6H$_2$O (180 mg, Co/Ni molar ratio 1:1), and urea (276 mg) were dissolved into the GO colloidal solution (10 mL, 2 mg mL^{-1} in water) under vigorous stirring and ultrasonication for 30 min, the solution was then transferred into a Teflon-lined stainless steel autoclave and kept at 150 °C for 24 h. The as-synthesized G–CH composites were washed with deionized water for several times, and then monolithic G–CH composite film was fabricated by the vacuum filtration method. For a typical run, the composite solution (50 mL, 0.25 mg mL^{-1}) was treated for 15 min under ultrasonic

conditions and filtered by a mixed cellulose ester membrane (0.22 µm pore size). The as-obtained filter cake was then dried in air at room temperature for 12 h to get a free-standing composite film, of which the thickness can be controlled by changing the volume of the G–CH composite solution. For the G–CH–CNT composite films, CNTs used in this work was treated by acid oxidation reported in previous work,[21] and then the desired amount of CNTs were dispersed in water under continuing ultrasonic for 15 min to make a solution (0.3 mg mL^{-1}). After that, the CNT dispersion (10 mL) was mixed with G–CH composites solution (50 mL) under vigorous stirring for 10 min. The G–CH–CNT composite films were also made by vacuum filtration. For comparison, the NiCo–CH species were also prepared under the same conditions in the absence of GO.

Materials Characterization: The as-obtained samples were examined by FE–SEM (FEI NOVA NanoSEM 450), TEM (Tecnai G220), and HR–TEM (JEOL 2100F), XRD (Cu Kα, λ = 1.5406 Å), FT-IR, Raman spectrum and XPS. The resistance of the samples was measured by the four probe method with Keiyhley 2400.

Electrochemical Characterization: The electrochemical properties of the samples were evaluated by a CHI 760D electrochemical workstation in a three-electrode cell in 6 M KOH aqueous electrolyte, in which platinum foil and Hg/HgO electrodes were used as the counter and reference electrodes, respectively. The working electrode was fabricated by directly pressing monolithic composite film onto nickel foams. For comparison, the slurry-derived powder electrode (G–CH–P) was prepared by mixing the G–CH composite powder, carbon black, and poly (tetrafluoroethylene) with ethanol in a mass ratio of 80:15:5. Then, the mixture was dried at 100 °C overnight under vacuum and then was pressed onto nickel foams to make electrodes.

Supporting Information

Supporting Information is available from the Wiley Online Library or from the author.

Acknowledgements

[1] P. G. Bruce, S. A. Freunberger, L. J. Hardwick, J. M. Tarascon, *Nat. Mater.* **2012**, *11*, 19.

[2] J. Chmiola, C. Largeot, P. L. Taberna, P. Simon, Y. Gogotsi, *Science* **2010**, *328*, 480.

[3] R. D. Smith, M. S. Prevot, R. D. Fagan, Z. Zhang, P. A. Sedach, M. K. Siu, S. Trudel, C. P. Berlinguette, *Science* **2013**, *340*, 60.

[4] J. R. Miller, P. Simon, *Science* **2008**, *321*, 651.

[5] P. Simon, Y. Gogotsi, *Nat. Mater.* **2008**, *7*, 845.

[6] Y. Wang, Y. Xia, *Adv. Mater.* **2013**, *25*, 5336.

[7] V. Augustyn, J. Come, M. A. Lowe, J. W. Kim, P. L. Taberna, S. H. Tolbert, H. D. Abruña, P. Simon, B. Dunn, *Nat. Mater.* **2013**, *12*, 518.

[8] X. Lu, T. Zhai, X. Zhang, Y. Shen, L. Yuan, B. Hu, L. Gong, J. Chen, Y. Gao, J. Zhou, Y. Tong, Z. L. Wang, *Adv. Mater.* **2012**, *24*, 938.

[9] X. Lu, M. Yu, G. Wang, Y. Tong, Y. Li, *Energy Environ. Sci.* **2014**, *7*, 2160.

[10] Z. Niu, J. Chen, H. H. Hng, J. Ma, X. Chen, *Adv. Mater.* **2012**, *24*, 4144.

[11] Y. Xu, Z. Lin, X. Huang, Y. Wang, Y. Huang, X. Duan, *Adv. Mater.* **2013**, *25*, 5779.

[12] Z. S. Wu, K. Parvez, X. Feng, K. Mullen, *Nat. Commun.* **2013**, *4*, 2487.

[13] L. L. Zhang, X. Zhao, M. D. Stoller, Y. Zhu, H. Ji, S. Murali, Y. Wu, S. Perales, B. Clevenger, R. S. Ruoff, *Nano Lett.* **2012**, *12*, 1806.

[14] Z. S. Wu, K. Parvez, A. Winter, H. Vieker, X. Liu, S. Han, A. Turchanin, X. Feng, K. Mullen, *Adv. Mater.* **2014**, *26*, 4552.

[15] Z. S. Wu, A. Winter, L. Chen, Y. Sun, A. Turchanin, X. Feng, K. Mullen, *Adv. Mater.* **2012**, *24*, 5130.

[16] Q. Lu, J. G. Chen, J. Q. Xiao, *Angew. Chem. Int. Ed.* **2013**, *52*, 1882.

[17] J. Jiang, Y. Li, J. Liu, X. Huang, C. Yuan, X. W. Lou, *Adv. Mater.* **2012**, *24*, 5166.

[18] H. Chen, L. Hu, M. Chen, Y. Yan, L. Wu, *Adv. Funct. Mater.* **2014**, *24*, 934.

[19] L. Wang, Z. H. Dong, Z. G. Wang, F. X. Zhang, J. Jin, *Adv. Funct. Mater.* **2013**, *23*, 2758.

[20] H. Wan, J. Jiang, Y. Ruan, J. Yu, L. Zhang, H. Chen, L. Miao, S. Bie, *Part. Part. Syst. Charact.* **2014**, *31*, 857.

[21] J. Yang, C. Yu, X. Fan, Z. Ling, J. Qiu, Y. Gogotsi, *J. Mater. Chem.* **2013**, *1*, 1963.

[22] C. Yu, J. Yang, C. Zhao, X. Fan, G. Wang, J. Qiu, *Nanoscale* **2014**, *6*, 3097.

[23] J. Yan, Z. Fan, W. Sun, G. Ning, T. Wei, Q. Zhang, R. Zhang, L. Zhi, F. Wei, *Adv. Funct. Mater.* **2012**, *22*, 2632.

[24] Y. Jiang, P. Wang, X. Zang, Y. Yang, A. Kozinda, L. Lin, *Nano Lett.* **2013**, *13*, 3524.

[25] H. P. Cong, X. C. Ren, P. Wang, S. H. Yu, *Energy Environ. Sci.* **2013**, *6*, 1185.

[26] A. Sumboja, C. Y. Foo, X. Wang, P. S. Lee, *Adv. Mater.* **2013**, *25*, 2809.

[27] C. Y. Foo, A. Sumboja, D. Jia, H. Tan, J. Wang, P. S. Lee, *Adv. Energy Mater.* **2014**, *4*, 1400236.

[28] Y. Cheng, H. Zhang, C. V. Varanasi, J. Liu, *Energy Environ. Sci.* **2013**, *6*, 3314.

[29] M. Li, Z. Tang, M. Leng, J. Xue, *Adv. Funct. Mater.* **2014**, *24*, 7495.

[30] Y. He, W. Chen, X. Li, Z. Zhang, J. Fu, C. Zhao, E. Xie, *ACS Nnao* **2013**, *7*, 174.

[31] C. Wang, J. Xu, M.-F. Yuen, J. Zhang, Y. Li, X. Chen, W. Zhang, *Adv. Funct. Mater.* **2014**, *24*, 6372.

[32] G. Zhang, X. W. Lou, *Sci. Rep.* **2013**, *3*, 1470.

[33] J. Xiao, S. Yang, *J. Mater. Chem.* **2012**, *22*, 12253.

[34] J. Yang, C. Yu, X. Fan, J. Qiu, *Adv. Energy Mater.* **2014**, *4*, 1400761.

[35] S. Chen, S.-Z. Qiao, *ACS Nano* **2013**, *7*, 10190.

[36] B. P. Bastakoti, Y. Kamachi, H.-S. Huang, L.-C. Chen, K. C. W. Wu, Y. Yamauchi, *Eur. J. Inorg. Chem.* **2013**, *2013*, 39.

[37] H. Chen, J. Jiang, L. Zhang, H. Wan, T. Qi, D. Xia, *Nanoscale* **2013**, *5*, 8879.

[38] Z. Lei, L. Lu, X. S. Zhao, *Energy Environ. Sci.* **2012**, *5*, 6391.

[39] J. Yan, W. Sun, T. Wei, Q. Zhang, Z. Fan, F. Wei, *J. Mater. Chem.* **2012**, *22*, 11494.

[40] Y. Fang, B. Luo, Y. Jia, X. Li, B. Wang, Q. Song, F. Kang, L. Zhi, *Adv. Mater.* **2012**, *24*, 6348.

[41] C. Guan, J. Liu, C. Cheng, H. Li, X. Li, W. Zhou, H. Zhang, H. J. Fan, *Energy Environ. Sci.* **2011**, *4*, 4496.

[42] D. Yang, A. Velamakanni, G. Bozoklu, S. Park, M. Stoller, R. D. Piner, S. Stankovich, I. Jung, D. A. Field, C. A. Ventrice, R. S. Ruoff, *Carbon* **2009**, *47*, 145.

[43] C. Yuan, J. Li, L. Hou, X. Zhang, L. Shen, X. W. D. Lou, *Adv. Funct. Mater.* **2012**, *22*, 4592.

[44] A. Vlad, N. Singh, J. Rolland, S. Melinte, P. M. Ajayan, J. F. Gohy, *Sci. Rep.* **2014**, *4*, 4315.

[45] Y. Meng, K. Wang, Y. Zhang, Z. Wei, *Adv. Mater.* **2013**, *25*, 6985.

[46] B. G. Choi, S. J. Chang, H. W. Kang, C. P. Park, H. J. Kim, W. H. Hong, S. Lee, Y. S. Huh, *Nanoscale* **2012**, *4*, 4983.

[47] Y. Cheng, S. Lu, H. Zhang, C. V. Varanasi, J. Liu, *Nano Lett.* **2012**, *12*, 4206.

[48] S. Chen, J. Duan, Y. Tang, S. Zhang Qiao, *Chem. Eur. J.* **2013**, *19*, 7118.

[49] C. Shang, S. Dong, S. Wang, D. Xiao, P. Han, X. Wang, L. Gu, G. Cui, *ACS Nano* **2013**, *7*, 5430.

[50] W. S. Hummers, R. E. Offeman, *J. Am. Chem. Soc.* **1958**, *80*, 1339.